Identification and analysis of ground surface rupture patterns from thrust and reverse fault earthquakes using geomechanical models

Kristen Chiama [i], William Bednarz [ii], Robb Moss [iii], and John H. Shaw [iv]

i) PhD Candidate, Department of Earth and Planetary Sciences, Harvard University, 20 Oxford St, Cambridge, Massachusetts, 02138 United States of America.
ii) Graduate Student, Department of Computer Science, Brown University, 115 Waterman St, Providence, Rhode Island, 02906, United States of America.
iii) Professor, Department of Civil and Environmental Engineering, California Polytechnic State University, San Luis Obispo, California 93407, United States of America.
iv) Professor, Department of Earth and Planetary Sciences, Harvard University, 20 Oxford St, Cambridge, Massachusetts, 02138, United States of America.

ABSTRACT

We define the physical processes that control the style and distribution of ground surface ruptures on thrust and reverse faults during large magnitude earthquakes through an expansive suite of geomechanical models developed with the distinct element method (DEM). Our models are based on insights from analog sandbox fault experiments as well as coseismic ground surface ruptures in historic earthquakes. DEM effectively models the geologic processes of faulting at depth in cohesive rocks, as well as the granular mechanics of soil and sediment deformation in the shallow subsurface. We developed an initial suite of 45 2D DEM experiments on dense, 5.0 m thick sediment in a model 50 m wide with a fault positioned 20 m from the driving wall and slipped each model at a constant rate (0.3 m/s) from 0 to 5.0 m. We evaluated a range of homogeneous sediment mechanics (cohesion and tensile strength from 0.1 to 2.0 MPa) across a range of fault dip angles. In addition, we examined various depths of sediment above the fault tip. Based on these experiments, we developed a classification system of the observed fault scarp morphology including three main types (monoclinal, pressure ridge, and simple scarps), each of which can be subsequently modified by hanging wall collapse. After this initial suite of models, we generated an additional 2,981 experiments of homogeneous and heterogeneous sediment in dense, medium-dense, and loosely packed sediment across a wide range of sediment depths and mechanics, as well as a range of fault dips (20 – 70º). These models provide robust statistical relationships between model parameters such as the fault dip and sediment strength mechanics with the observed surface deformation characteristics, including scarp height, width, and dip as well as the tendency for secondary fault splays. These relationships are supported by natural rupture patterns from recent and paleo-earthquakes across a range of geologic settings. In conjunction with these natural examples, our models provide a basis to more accurately forecast ground surface deformation characteristics that will result from future earthquakes based on limited information about the earthquake source and local sediment properties.

Keywords: distinct element method, surface fault rupture, fault scarps, tectonic geomorphology, numerical modeling.

1 INTRODUCTION

Large magnitude thrust and reverse fault earthquakes feature diverse styles of surface ruptures that can have a major impact on our infrastructure. Ground surface warping, vertical offsets, and distributed deformation – including fault splays and backthrusts – observed in these events pose substantial hazards towards our energy transmission and telecommunication systems, transportation networks, as well as industrial and residential infrastructure (Kelson et al., 2001; Petersen et al., 2011; Chang et al., 2015; Boncio et al., 2018; Bray et al., 2019; Baize et al., 2020). Recent examples of large magnitude earthquakes with substantial impacts on infrastructure include the 1999 M 7.6 Chi-Chi, Taiwan and 2016 M 7.8 Kaikoura, New Zealand in Figure 1 (Chen et al., 2001; Bayer 2017).

The ability to forecast and prepare for ground surface rupture in thrust and reverse fault earthquakes currently relies largely on Probabilistic Fault Displacement Hazards Assessment (PFDHA) analysis, which provided a probability of exceedance over a time frame for specific ground rupture characteristics (Wells and Coppersmith, 1994; Youngs et al., 2003; Petersen et al., 2011). These relationships are informed by natural historical ruptures (Moss and Ross, 2011; Moss et al.,

https://doi.org/10.3208/jgssp.v10.OS-15-06

2018; Sarmiento et al., 2021; Chiama et al., 2023). As an example, the Trans-Alaskan pipeline withstood 5.5 m of right-lateral strike-slip offset during the 2002 M 7.9 Denali earthquake based on engineering design informed by PFDHA analysis (Cluff et al., 2003; Sorensen and Meyer, 2003). Nevertheless, these hazard estimates are based on a small dataset of historic events and thus may not capture the full range of potential surface rupture morphologies that can occur in future earthquakes.

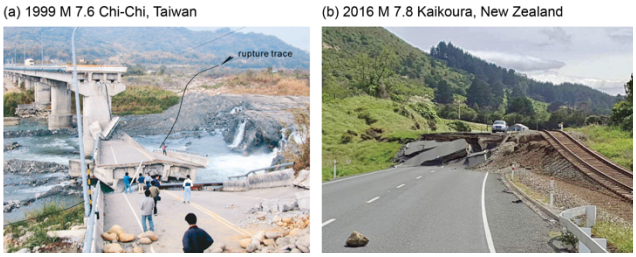

Fig. 1. Images of surface ruptures associated with coseismic thrust and reverse-fault displacements: (a) 1999 M 7.6 Chi-Chi, Taiwan, earthquake (Chen et al., 2001); and (b) 2016 M 7.8 Kaikoura, New Zealand, earthquake (Bayer, 2017).

Based on the methods and models presented in Chiama et al. (2023), we use the distinct element method (DEM) to investigate the patterns of potential ground surface ruptures that result due to slip on a fault, as a function of the fault dip, the sediment strength mechanics, and the depth of unruptured sediment to the fault tip. We evaluate the surface deformation characteristics (deformation zone width, vertical displacement, scarp dip) of these models using computer vision techniques such as image masking, signal processing, and specialized feature extraction tailored to the specific scarp types. Our goal is to provide robust statistical relationships between model parameters and the resultant ground surface deformation that can be used to inform both probabilistic and deterministic approaches to assessing ground rupture hazards.

2 METHODS

Geomechanical models using the discrete and distinct element methods effectively reproduce the kinematics and behavior of faults and folding through varying media of sedimentary layers to basement rocks and have been used in a wide variety of applications to simulate geological processes (Morgan, 1999, 2004; Erickson et al., 2001; Strayer and Suppe, 2002; Finch et al., 2003; Guo and Morgan, 2004; Imber et al., 2004; Hardy and Finch, 2006, 2007; Hughes et al., 2014; Morgan, 2015; Garcia & Bray, 2018a,b; Hughes 2020). We use Particle Flow Code (PFC2D) version 7.00 for our experiments based on the work by Cundall and Strack (1979). Based on the models presented in the 2D DEM models in Chiama et al. (2023), we employed similar model boundary conditions (Fig. 4) with sediment mechanics calibrated to the analog sandbox fault models presented in Cole & Lade (1984) and Bransby et al. (2008) as well as the 3D DEM models from Garcia & Bray (2018b).

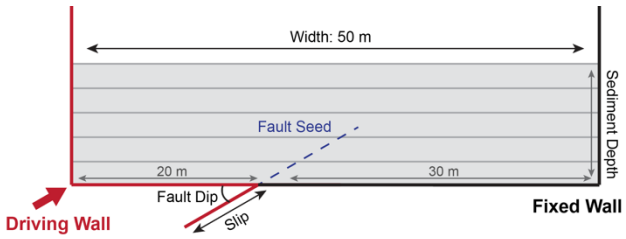

Fig. 2. DEM model geometry and boundaries (not to scale).

We used a 2D DEM model of thrust and reverse fault earthquakes that is 50 m wide with a fault plane that displaces the hanging wall (see Fig. 2, driving wall) upwards by a prescribed amount of continuous slip (0 to 5 m) at a rate of 0.3 m/s to produce ground surface deformation. The sediment consists of 50x sand-sized particles (0.025 – 0.06625 m radii). We constructed dense, medium-dense, and loose assemblages by changing the initial friction coefficient (μ_{int}) during the gravitational settling of particles based on the method of Garcia & Bray (2018a). The friction coefficient (μ) is reset to a standard value of 0.3 prior to the deformation sequence. The particles were bonded using the parallel contact bond model from Itasca (1999) with prescribed values of cohesion and tensile strengths. Biaxial stress tests of the bonded material were used to calibrate the contact bonds to natural properties of near-surface sediment (Table 1 & 2). Table 1 reports the relationship of sediment assemblage density to the DEM model parameter μ_{int}. Table 2 reports the sediment density and contact bond strength (cohesion equal to tensile strength) relative to the measured Young's Modulus, failure angle (θ), friction angle (φ), and measured bulk friction coefficient (μ_{bulk}).

Prior to deformation, we implemented a "fault seed" which propagates a plane of weakness into the sediment at the given fault dip. This represents a case where a fault plane has developed from previous earthquakes. The fault seed avoids undesirable boundary condition effects and allows us to test the depth of unruptured sediment above the fault tip as a variable without regenerating the sediment for each experiment which is computationally expensive (Chiama et al., 2023).

Table 1. DEM Sediment Assemblage Properties.

Sediment Assemblage	μ_{int}	Porosity	Void Ratio
Dense	0	0.15	0.18
Medium	0.25	0.17	0.21
Loose	0.5	0.19	0.23

For our experiments, we tested 9 sediment assemblages of 3, 5, and 10 m depth of dense, medium, and loose sediment across a range of homogeneous and heterogeneous sediment mechanics. The homogeneous cases are defined as experiments where every

sedimentary layer has the same sediment mechanics whereas heterogenous cases can have different sediment mechanics per sedimentary unit. For the homogeneous experiments, we evaluated cases where the cohesive and tensile strength of the contact bonds are equal to one another (0.1, 0.5, 1.0, 1.5, 2.0 MPa), where cohesive strength is held constant (cohesion: 1.0 MPa, tensile strength: 0.1, 0.5, 1.0, 1.5, 2.0 MPa), and where tensile strength is held constant (tensile strength: 1.0 MPa, cohesion: 0.1, 0.5, 1.0, 1.5, 2.0 MPa). For heterogeneous experiments, we set the cohesive and tensile strength equal to one another for each sedimentary unit and varied the strength of units from the base of the model to the surface in a vertical gradient. We tested 3 cases for each sediment assemblage of weak, moderate, and strong sediment mechanics with the strongest units at the base of the model. Finally, we tested a range of fault dips 20º, 30º, 40º, 45º, 50º, 60º, and 70º and varied the amount of unruptured sediment above the fault tip (e.g., 0.75, 1.25, 1.5, 2.25, 2.5, 2.75, 5, and 7.5 m) with the fault seed as a function of the total sediment depth (e.g., 25%, 50%, and 75% of 3, 5, and 10 m depth). This range of parameters comprise a total of 2,459 homogeneous experiments and 567 heterogenous experiments.

Table 2. DEM Parameters & Measured Bulk Material Properties.

Sediment	Contact Bond Strength (MPa)	Young's Modulus (MPa)	θ (º)	φ (º)	μ_{bulk}
Dense	0.1	8.83	62.0	34.0	0.68
	0.5	11.99	63.5	37.0	0.75
	1.0	14.02	60.0	30.0	0.58
	1.5	16.72	60.0	30.0	0.58
	2.0	17.43	61.0	32.0	0.63

We evaluated the model results using computer vision (CV) techniques since each experiment outputs an image of the model deformation every 500 cycles in the DEM code. This is equivalent to ~ 4.5 mm of slip on the fault, yielding ~1,114 images of deformation for each experiment, and a total of ~2,739,326 images of the homogeneous experiments and ~631,638 images of the heterogeneous experiments. We measured the surface scarp characteristics such as the deformation zone width, scarp dip, and the uplift every 0.05 m of slip on the fault at depth from 0 to 5 m of total accumulated slip.

After pre-processing each image, we performed surface extraction and smoothing procedures to eliminate noise. Subsequently, our CV model delineated deformation zone boundaries and located the top scarp point. The analysis identified abrupt, blocky alterations in the surface, indicative of collapse. Our object detection algorithm then highlighted segments of the hanging wall that had collapsed. In addition to this, we scrutinized the outline of the hanging wall to identify overhangs, characterized by negative angles, a distinctive trait of simple scarps. These features played a pivotal role in automating the calculation of crucial parameters from the slip images, such as the scarp angle, deformation zone width, and scarp height. Measurements were taken using pixel dimensions and converted back to meters for analysis.

Based on the empirical relationships of Biasi and Weldon (2006):

$$M = 6.94 + 1.14 \cdot \log(d_{ave}) \quad (1)$$

where M is the magnitude of an earthquake and d_{ave} is the average displacement, we relate displacement in our DEM models to earthquake magnitude. Our models evaluate slip ranges from 0.05 m to 5.0 m which corresponds to a range of earthquake magnitudes of M 5.46 to 7.74. We examined the DEM experiments output at intervals of 0.05 m of slip, yielding a total of 101 measurements of each DEM model.

3 RESULTS

3.1 Fault Scarp Classifications

The initial DEM experiments presented in Chiama et al. (2023) covered a range of sediment strengths (0.1 – 2.0 MPa: cohesion and tensile strength of contact bonds) and fault dips (20º, 40º, 60º) in dense, 5 m deep sediment which revealed a set of fault scarp morphologies that defined 3 main classes (monoclinal, pressure ridge, and simple) each with a modified case of hanging wall collapse (Fig. 3).

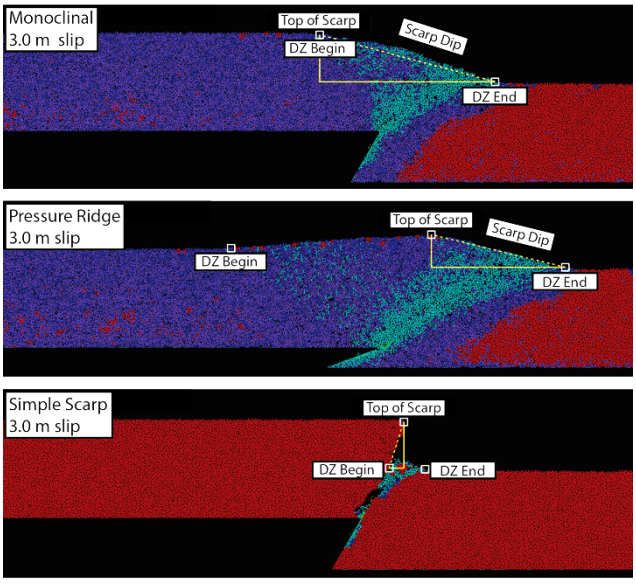

Fig. 3. CV model measurements of DEM experiments for a monoclinal (*top*), pressure ridge (*middle*), and simple scarp (*bottom*) based on the scarp type classifications presented in Chiama et al. (2023). DZ is deformation zone, white boxes indicate pixel locations derived by the CV model, and the dashed yellow line is the best scarp dip fit.

The monoclinal scarps are a single dip panel that grows in height and width with increasing slip on the fault at depth but maintains a surface scarp dip near the angle of repose. The pressure ridge scarps feature additional uplift above the top of the hanging wall as a

"pop up" structure, which is often associated with formation of a backthrust. The simple scarps were originally described by Philip et al. (1992) as the displacement of the hanging wall above the footwall in sufficiently cohesive sediment to resist hanging wall collapse. The simple scarps have a distinctive "Z" shape in morphology. Each of these 3 classifications have measurable differences in morphology based on the deformation zone (DZ) width, scarp height (U_s), uplift above the surface of the undeformed hanging wall (U_s - U_d), and average scarp dip.

Our CV model was trained on the initial 45 DEM experiments from Chiama et al. (2023). Figure 3 provides examples for each of the main scarp types indicating identifiable features and scarp measurements used to construct relationships between surface deformation characteristics and DEM model parameters such as fault dip, sediment strength, and estimated earthquake magnitude.

3.2 Fault Scarp Characteristics

The CV model results for the training dataset of 45 DEM experiments are reported below. Figure 4 shows the relationships between ground surface deformation characteristics (uplift, deformation zone width, and scarp dip) and the accumulation of slip on a fault at depth converted to an estimated earthquake magnitude (Biasi and Weldon, 2006) based on fault scarp types. The accumulation of slip is the slip consumed by the DEM model from 0 to 5.0 m at the prescribed fault dip angle.

The pressure ridge and their correlated collapse features report substantial uplift above to top of the undeformed hanging wall and often occur on low angle faults (20º) in Figure 4a. The collapse features are more prevalent in stronger sediment (1.5 and 2.0 MPa) at higher magnitudes while the standard pressure ridge features tend to occur in weak to moderate strength sediment (0.1 – 1.0 MPa) across all magnitudes. Monoclinal and simple scarps do not feature this additional uplifted region and therefore these measurements cluster near 0.0 m (Fig. 4a). There is a wide range of deformation widths measured across the DEM experiments (Fig. 4b). Pressure ridges have the widest deformation zones, up to 18.24 m in weak sediment on a low angle fault. In contrast, simple scarps have the smallest deformation zone width which is the product of the horizontal displacement accumulated at depth on the fault (Fig. 4b). This is because the sediment is sufficiently strong (2.0 MPa) to resist hanging wall collapse and thus, their morphology is representative of the simple displacement of the hanging wall above the footwall. Meanwhile, monoclinal scarps maintain the angle of repose of the sediment and increase in width as the displacement on the fault at depth increases. Monoclinal scarps are most common on moderate to steep dipping faults (40º to 60º) in weak to moderate strength sediment. Further, simple scarps and their collapse versions are the only measured scarp types to exhibit a scarp overhang, yielding a negative scarp dip angle (Fig. 4c). Nevertheless, simple scarps often do not form until sufficient displacement has accumulated on the fault and often begin as a monoclinal scarp at low amounts of slip (Fig. 4c). Thus, Figure 4c shows that most simple scarps occur on steep faults (60º) in strong sediment (2.0 MPa) with > 7.0 magnitude earthquakes as these have sufficient displacement and sediment strength to support a fault overhang. This is supported by natural cases of simple scarps reported in the 2008 M 7.9 Wenchuan earthquake and the 2016 M 7.8 Kaikoura earthquake (Li et al., 2010; Nicol et al., 2018).

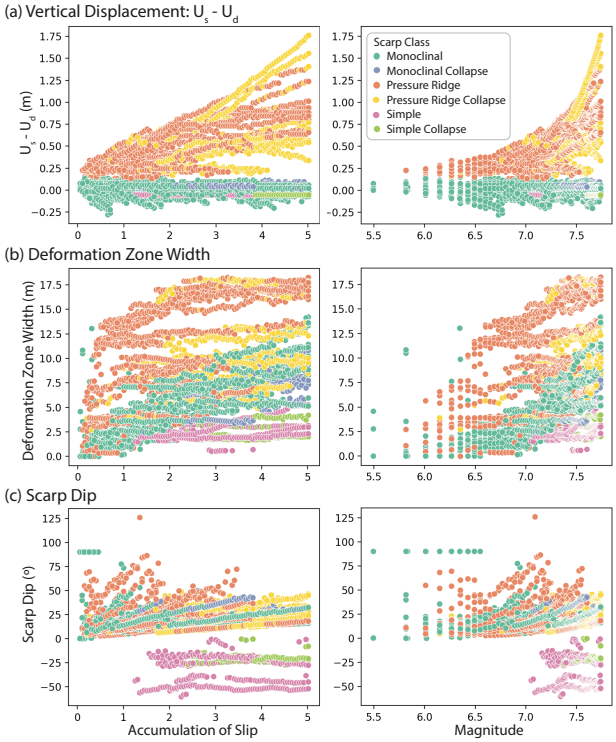

Fig. 4. CV model measurements of 45 DEM experiments based on the scarp type classifications presented in Chiama et al. (2023) plotted as surface measurements by the accumulation of slip on the fault at depth (*left*) and the estimated magnitude of earthquake calculated from Biasi and Weldon (2006) (*right*). (a) Vertical displacement as a function of U_s – U_d. (b) Deformation zone width. (c) Scarp dip angle.

4 DISCUSSION

We can use these measurements of surface deformation to construct predictive relationships of model parameters, such as fault dip and sediment strength, with scarp type and distribution of surface deformation features. Despite the additional uplift observed in pressure ridges, the monoclinal and pressure ridge scarps have the lowest measured overall scarp heights while their collapse versions and simple scarps tend to have higher scarp heights related to the vertical displacement at depth on steeper faults (Fig. 4a). Most of the DEM experiments feature a scarp dip angle within 0 to 50º since the angle of repose is ~32.6º (Fig. 4c).

Nevertheless, simple and simple collapse scarps with the fault scarp overhang have negative dip angles (Fig. 4c). There are a few notable monoclinal experiments that report a scarp dip of 90º at low intervals of slip. This is due to the limitations of the CV model to measure small changes in surface deformation.

Figure 5 shows the distributions of deformation zone widths for each of the fault scarp types which can inform fault displacement hazard assessments. Simple and simple collapse scarps have the smallest deformation zone widths while, as expected, pressure ridges and their collapse version have the widest zone of deformation. The deformation zone width of the monoclinal scarps and their collapse case are related to the angle of repose of the sediment and increasing slip on the fault at depth. Distributions such as the one shown below are useful in hazard assessments.

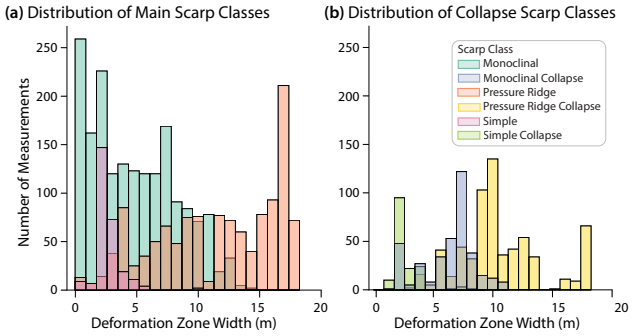

Fig. 5. Distributions of the deformation zone width organized by the (a) main scarp type classifications and (b) collapse-modified scarp classes presented in Chiama et al. (2023).

4.1 Benefits and Limitations of the CV Model

By applying the CV model to take measurements of the PNG files output by the DEM model experiments, we can achieve a much higher resolution of ground surface characteristics and flag changes in morphology, such as the initiation of collapse features. While the scarp characteristics were measured every 0.5 m of slip in Chiama et al. (2023), the CV model offers much higher resolution with measurements taken up to every 0.05 m of displacement on the fault. Nevertheless, given such a high resolution, there are often minimal changes in the surface deformation between PNG files and the CV model struggles with the first few images of slip in an experiment (i.e., at low slip values). Thus, there are a few monoclinal scarps that report a scarp dip of 90º at low intervals of slip (Fig. 4c). Once a scarp type has been established, after ~0.35 m of slip, the accuracy and precision of the CV model defining scarp measurements increases substantially. The measurements of each experiment have an uncertainty of up to ± 0.0135 m.

4.2 Application to PFDHA

These DEM experiments show promise to supplement current PFDHA efforts. Current hazard assessments are based on 25 measured historical ruptures (Sarmiento et al., 2021). DEM models can fill in the gaps of our knowledge and provide a reproducible, robust method of providing site characterizations. Further, we can develop statistical relationships on the suite of DEM models to forecast potential ground surface deformation.

5 CONCLUSIONS

We produced a large suite of DEM experiments of thrust and reverse fault earthquakes across a range of sediment strengths, depths, and fault dips. We report a CV model that has been trained on 45 DEM experiments with a range of surface deformation characteristics such as monoclinal, pressure ridge, and simple scarps. The resultant ground surface deformation is dependent on the sediment strength and prescribed fault dip. Low angle fault (20º) in weak to moderate strength sediment yield pressure ridges while their collapse version occurs in strong sediment, both of which have additional uplift above the undeformed top of the hanging wall and the widest deformation zones. Moderate faults (40º) yield monoclinal scarps that increase in height, width, and scarp dip to maintain the angle of repose in weak to moderate sediment with increasing displacement on the fault at depth. High angle faults (60º) in strong sediment yield simple scarps that resist hanging wall collapse and have the smallest deformation zone widths. DEM experiments of earthquakes show promise in characterizing surface deformation to aid in PFDHA analysis based on site characterization of fault dip and sediment strengths.

ACKNOWLEDGEMENTS

This research was supported by the National Science Foundation (NSF), Division of Earth Sciences (EAR), Tectonics Program, Grant Number 2207119. We thank F. Estefan Garcia, Michael Naylor Hudgins, Brendan Meade, Emily Carrero Mustelier, Andreas Plesch, Natasha Toghramadjian, and Robert M. Welch for thoughtful discussions and coding suggestions.

REFERENCES

1) Baize, S., Nurminen, F., Sarmiento, A., Dawson, T., Takao, M., Scotti, O., et al. (2020). A worldwide and unified database of surface ruptures (SURE) for fault displacement hazard analyses. *Seismological Research Letters*, *91*(1), 499–520. https://doi.org/10.1785/0220190144.

2) Bayer, K. (12 Nov 2017). Mixed emotions in Kaikoura ahead of massive magnitude-7.8 quake's one-year anniversary. *New Zealand Herald*. https://www.nzherald.co.nz/nz/mixed-emotions-in-kaikoura-ahead-of-massive-magnitude-78-quakes-one-year-anniversary/INRZHEHBOMLQBM7GTJUFGWP7CY/.

3) Biasi, G. P., & R. J. Weldon (2006). Estimating surface rupture length and magnitude of paleoearthquakes from point measurements of rupture displacement, *Bulletin of the Seismological Society of America,* 96(5), 1612–1623.

4) Boncio, P., Liberi, F., Caldarella, M., & Nurminen, F. C. (2018). Width of surface rupture zone for thrust earthquakes: Implications for earthquake fault zoning. *Natural Hazards and Earth System Sciences*, *18*(1), 241–256. https://doi.org/10.5194/nhess-18-241-2018.

5) Bransby, M. F., Davies, M. C. R., El Nahas, A., & Nagaoka, S. (2008). Centrifuge modelling of reverse fault-foundation interaction. *Bulletin of Earthquake Engineering*, *6*(4), 607–628. https://doi.org/10.1007/s10518-008-9080-7.

6) Bray, J. D., Frost, J. D., Rathje, E. M., & Garcia, F. E. (2019). Recent advances in geotechnical post-earthquake reconnaissance. *Frontiers in Built Environment*, *5*(January), 1–12. https://doi.org/10.3389/fbuil.2019.00005.

7) Chang, Y. Y., Lee, C. J., Huang, W. C., Hung, W. Y., Huang, W. J., Lin, M. L., & Chen, Y. H. (2015). Evolution of the surface deformation profile and subsurface distortion zone during reverse faulting through overburden sand. *Engineering Geology*, *184*, 52–70. https://doi.org/http://dx.doi.org/10.1016/j.enggeo.2014.10.023

8) Chen, W., Huang, B., Chen, Y., Lee, Y., et al., (2001). 1999 Chi-Chi earthquake: A case study on the role of thrust-ramp structures for generating earthquakes. *Bulletin of the Seismological Society of America, 91(5),* 986-994. doi: 10.1785/0120000731.

9) Chiama, K., Chauvin, B., Plesch, A., Moss, R., Shaw, J.H. (2023) Geomechanical modeling of ground surface deformation associated with thrust and reverse ‐ fault earthquakes: A distinct element approach. *Bulletin of the Seismological Society of America*, 113(4), 1702–1723, https://doi.org/10.1785/0120220264.

10) Cluff, L. S., Page, R. A., Slemmons, D. B., & Crouse, C. B. (2003). Seismic hazard exposure for the Trans-Alaska pipeline. In *Sixth U.S. Conference and Workshop on Lifeline Earthquake Engineering, ASCE Technical Council on Lifeline Earthquake Engineering*, Long Beach, CA.

11) Cole, D. A., & Lade, P. V. (1984). Influence zones in alluvium over dip-slip faults. *Journal of Geotechnical Engineering*, *110*(5), 599–615. https://doi.org/10.1061/(ASCE)0733-9410(1984)110:5(599).

12) Cundall, P. A., & Strack, O. D. L. (1979). A discrete numerical model for granular assemblies. *Geotechnique*, *29*(1), 47–65.

13) Erickson, S. G., Strayer, L. M., & Suppe, J. (2001). Initiation and reactivation of faults during movement over a thrust-fault ramp: Numerical mechanical models. *Journal of Structural Geology*, *23*(1), 11–23. https://doi.org/10.1016/S0191-8141(00)00074-2.

14) Finch, E., Hardy, S., & Gawthorpe, R. (2003). Discrete element modelling of contractional fault- propagation folding above rigid basement fault blocks. *Journal of Structural Geology*, *25*(4), 515–528. https://doi.org/10.1016/S0191-8141(02)00053-6.

15) Garcia, F. E., & Bray, J. D. (2018a). Distinct element simulations of earthquake fault rupture through materials of varying density. *Soils and Foundations*, *58*(4), 986–1000. https://doi.org/10.1016/j.sandf.2018.05.009.

16) Garcia, F. E., & Bray, J. D. (2018b). Distinct Element Simulations of Shear Rupture in Dilatant Granular Media. *International Journal of Geomechanics*, *18*(9), 04018111. https://doi.org/10.1061/(asce)gm.1943-5622.0001238.

17) Guo, Y., & Morgan, J. K. (2004). Influence of normal stress and grain shape on granular friction: Results of discrete element simulations. *Journal of Geophysical Research: Solid Earth*, *109*(12), 1–16. https://doi.org/10.1029/2004JB003044.

18) Hardy, S., & Finch, E. (2006). Discrete element modelling of the influence of cover strength on basement-involved fault-propagation folding. *Tectonophysics*, *415*(1–4), 225–238. https://doi.org/10.1016/j.tecto.2006.01.002.

19) Hardy, S., & Finch, E. (2007). Mechanical stratigraphy and the transition from trishear to kink-band fault-propagation fold forms above blind basement thrust faults: A discrete-element study. *Marine and Petroleum Geology*, *24*(2), 75–90. https://doi.org/10.1016/j.marpetgeo.2006.09.001.

20) Hughes, A. N. (2020). Mechanical controls on structural styles in shortening environments: A discrete-element modelling approach. *Geological Society Special Publication*, *490*(1), 33–55. https://doi.org/10.1144/SP490-2019-114.

21) Hughes, A. N., Benesh, N. P., & Shaw, J. H. (2014). Factors that control the development of fault-bend versus fault-propagation folds: Insights from mechanical models based on the discrete element method (DEM). *Journal of Structural Geology*, *68*(PA), 121–141. https://doi.org/10.1016/j.jsg.2014.09.009.

22) Imber, J., Tuckwell, G. W., Childs, C., Walsh, J. J., Manzocchi, T., Heath, A. E., Bonson, C. G., & Strand, J. (2004). Three-dimensional distinct element modelling of relay growth and breaching along normal faults. *Journal of Structural Geology*, 26(10), 1897-1911.

23) Itasca (1999). *PFC2D: Theory and Background, User's Guide, Command Reference, FISH in PFC2D*. Minneapolis, MN, USA: Itasca Consulting Group.

24) Kelson, K. I., Kang, K. H., Page, W. D., Lee, C. T., & Cluff, L. S. (2001). Representative styles of deformation along the Chelungpu Fault from the 1999 Chi-Chi (Taiwan) earthquake: Geomorphic characteristics and responses of man-made structures. *Bulletin of the Seismological Society of America*, *91*(5), 930–952. https://doi.org/10.1785/0120000741.

25) Li, Y., D. Jia, J. H. Shaw, J. Hubbard, A. Lin, M. Wang, L. Luo, H. Li, and L. Wu (2010). Structural interpretation of the seismic faults of the Wenchuan earthquake: Three-dimensional modeling of the Longmen Shan fold-and-thrust belt, J. Geophys. Res. 115, no. 4, doi: 10.1029/2009JB006824.

26) Morgan, J. K. (1999). Numerical simulations of granular shear zones using the distinct element method: 2. Effects of particle size distribution and interparticle friction on mechanical behavior. *Journal of Geophysical Research: Solid Earth*, *104*(B2), 2721–2732. https://doi.org/10.1029/1998jb900055.

27) Morgan, J. K. (2004). Particle dynamics simulations of rate- and state-dependent frictional sliding of granular fault gouge. *Pure and Applied Geophysics*, *161*(9–10), 1877–1891. https://doi.org/10.1007/s00024-004-2537-y.

28) Morgan, J. K. (2015). Effects of cohesion on the structural and mechanical evolution of fold and thrust belts and contractional wedges: Discrete element simulations. *Journal of Geophysical Research: Solid Earth*, *120*, 3870–3896. https://doi.org/10.1002/2014JB011455.Received

29) Moss, R. E. S., & Ross, Z. E. (2011). Probabilistic fault displacement hazard analysis for reverse faults. *Bulletin of the Seismological Society of America*, *101*(4), 1542–1553. https://doi.org/10.1785/0120100248.

30) Moss, R. E. S., Buelna, M., & Stanton, K. V. (2018). Physical, analytical, and numerical modeling of reverse-fault displacement through near-surface soils. *Bulletin of the Seismological Society of America*, *108*(6), 3149–3159. https://doi.org/10.1785/0120180067.

31) Nicol, A., N. Khajavi, J. R. Pettinga, C. Fenton, T. Stahl, S. Bannister, K. Pedley, N. Hyland-Brook, T. Bushell, I. Hamling, et al. (2018). Preliminary geometry, displacement, and kinematics of fault ruptures in the epicentral region of the 2016 Mw 7.8 Kaikoura, New Zealand, earthquake, Bull. Seismol. Soc. Am. 108, no. 3B, 1521–1539, doi: 10.1785/0120170329.

32) Petersen, M. D., Dawson, T. E., Chen, R., Cao, T., Wills, C. J., Schwartz, D. P., & Frankel, A. D. (2011). Fault displacement hazard for strike-slip faults. *Bulletin of the Seismological Society of America*, *101*(2), 805–825. https://doi.org/10.1785/0120100035.

33) Philip, H., Rogozhin, E., Cisternas, A., Bousquet, J. C., Borisov, B., & Karakhanian, A. (1992). The Armenian earthquake of 1988 December 7: faulting and folding, neotectonics and palaeoseismicity. *Geophysical Journal International*, *110*(1), 141–158. https://doi.org/10.1111/j.1365-246X.1992.tb00718.x.

34) Sarmiento, A., Madugo, D., Bozorgnia, Y., Shen, A., Mazzoni, S., Lavrentiadis, G., et al. (2021). Report GIRS 2021-08 Fault Displacement Hazard Initiative Database. doi: 10.34948/N36P48.

35) Sorensen, S. P., Meyer, K. J. (2003). Effect of the Denali fault rupture on the Trans-Alaska Pipeline. In the *Sixth U.S. Conference and Workshop on Lifeline Earthquake Engineering, ASCE Technical Council on Lifeline Earthquake Engineering*, Long Beach, CA.

36) Strayer, L. M., & Suppe, J. (2002). Out-of-plane motion of a thrust sheet during along-strike propagation of a thrust ramp: A distinct-element approach. *Journal of Structural Geology*, *24*(4), 637–650. https://doi.org/10.1016/S0191-8141(01)00115-8.

37) Strayer, L. M., Erickson, S. G., & Suppe, J. (2004). Influence of growth strata on the evolution of fault-related folds – Distinct-element models. *AAPG Memoir*, *82*, 413–437.

38) Wells, D. L. & Coppersmith, K. J. (1994). New empirical relationships among magnitude, rupture length, rupture width, rupture area, and surface displacement. *Bulletin of the Seismological Society of America*, 84(4), 974-1002.

39) Youngs, R. R., Arabasz, W. J., Anderson, R. E., Ramelli, A. R., Ake, J. P., Slemmons, D. B., et al. (2003). A methodology for probabilistic fault displacement hazard analysis (PFDHA). *Earthquake Spectra*, *19*(1), 191–219. https://doi.org/10.1193/1.1542891.